Matthew J. Emes, Azadeh Jafari, Farzin Ghanadi, Maziar Arjomandi
Hinge and overturning moments due to unsteady heliostat pressure distributions in a turbulent atmospheric boundary layer
Solar Energy, 2019; 193:604-617

Final publication at: http://dx.doi.org/10.1016/j.solener.2019.09.097

Hinge and overturning moments due to unsteady heliostat pressure distributions in a turbulent atmospheric boundary layer

Matthew J. Emes*, Azadeh Jafari, Farzin Ghanadi, Maziar Arjomandi

Centre for Energy Technology, School of Mechanical Engineering, The University of Adelaide, SA 5005, Australia

Abstract

Non-uniform pressure distributions on the heliostat surface due to turbulence in the atmospheric boundary layer (ABL) have a significant impact on the maximum bending moments about the hinge of and pedestal base of a conventional pedestal-mounted heliostat. This paper correlates the movement of the centre of pressure due to the mean and peak pressure distributions with the hinge and overturning moment coefficients using high-frequency pressure and force measurements on a scale-model heliostat within two simulated ABLs generated in a wind tunnel. The positions of the centre of pressure were calculated for a range of heliostat elevation-azimuth configurations using a similar analogy to those in ASCE 7-02 for monoslope-roof buildings, ASCE 7-16 for rooftop solar panels, and in the literature on flat plates. It was found that the maximum hinge moment is strongly correlated to the centre of pressure movement from the heliostat central elevation axis. Application of stow and operating load coefficients to a full-scale 36 m^2 heliostat showed that the maximum hinge moment remains below the stow hinge moment at maximum operating design gust wind speeds of 29 m/s in a suburban terrain and 33 m/s in a desert terrain. The operating hinge moments at elevation angles above 45° are less than 60% of the stow loads with a constant 40 m/s design wind speed. The results in the current study can be used to determine heliostat configurations and appropriate design wind speeds in different terrains leading to the maximum design wind loads on the elevation drive and foundation.

Keywords: heliostat; hinge moment; overturning moment; pressure distribution; centre of pressure; turbulence

Nomenclature

A	Heliostat mirror area (m^2)
$\alpha_{\bar{U}}$	Power law velocity profile exponent
α	Elevation angle of heliostat mirror plane with respect to the horizontal (°)
β	Azimuth angle of wind with respect to frontal projected heliostat mirror plane (°)
c	Heliostat mirror chord length (m)
c_{Fx}	Drag force coefficient
c_{Fz}	Lift force coefficient
$c_{M_{Hx}}$	Hinge moment coefficient about the axis x_H
$c_{M_{Hy}}$	Hinge moment coefficient about the elevation axis y_H
c_{M_y}	Overturning moment coefficient about the axis y_b at the base of the heliostat pylon
C_p	Pressure coefficient
F_N	Net force normal to the heliostat surface (N)
F_{Hx}	Drag force on the heliostat surface (N)
F_z	Lift force on the heliostat surface (N)
G_u	Velocity gust factor
H	Elevation axis height of heliostat hinge above the ground (m)
I_u	Longitudinal turbulence intensity (%)
I_w	Vertical turbulence intensity (%)
l_p	Distance to the centre of pressure from the centre of the heliostat mirror plane (m)
l_{px}	Longitudinal distance to the centre of pressure from the y-axis of the heliostat (m)
l_{py}	Lateral distance to the centre of pressure from the x-axis of the heliostat (m)
L_u^x	Longitudinal integral length scale (m)
L_w^x	Vertical integral length scale (m)
M_{Hx}	Hinge moment on heliostat about the axis x_H (N·m)
M_{Hy}	Hinge moment on heliostat about the elevation axis y_H (N·m)
M_y	Overturning moment about the axis y_b at the base of the heliostat pylon (N·m)
ρ	Air density (kg/m^3)
p	Differential pressure between the upper and lower heliostat surfaces (Pa)
P_i^f	Pressure fluctuations on the upper heliostat surface (Pa)
P_i^b	Pressure fluctuations on the lower heliostat surface (Pa)
$\bar{U}(z)$	Mean velocity profile (m/s)
$\bar{U}_H$	Mean velocity at heliostat elevation axis height (m/s)
$\hat{U}_{op}$	Operating gust wind speed at a 10-m height for heliostat design (m/s)
$\hat{U}_{st}$	Stow gust wind speed at a 10-m height for heliostat design (m/s)
x	Dimension parallel to the elevation axis on the heliostat mirror plane (m)
x_H	Longitudinal axis at the heliostat hinge height (m)
x_b	Longitudinal axis at the base of the heliostat pylon (m)
y	Dimension perpendicular to the elevation axis on the heliostat mirror plane (m)

y_H Lateral axis at the heliostat hinge height (m)

y_b Lateral axis at the base of the heliostat pylon (m)

z Vertical azimuth axis of heliostat (m)

z_0 Surface roughness height of logarithmic velocity profile (m)

1. Introduction

The development of concentrating solar thermal (CST) as an emerging renewable technology in recent decades has been accompanied by the increased deployment of large-scale power tower (PT) plants. A large number of heliostats are required to achieve the high temperatures and power cycle efficiencies in a central receiver PT plant (IEA-ETSAP and IRENA 2013), such that the heliostat field represents the largest contribution of almost half of the plant's total cost (Kolb *et al.* 2011; Pfahl *et al.* 2017b). The economic viability of PT systems relies on the reduction of the overall heliostat cost per unit area. For instance, lowering the strength and stiffness requirements, following a three-halves power law with the heliostat area (Kolb *et al.* 2011), can be achieved through the manufacturing of lighter wind-sensitive components of heliostats (Téllez *et al.* 2014; Emes *et al.* 2015). The elevation and azimuth drives, pedestal, foundation and mirror support structure of a conventional elevation-azimuth heliostat account for up to 80% of the heliostat capital cost (Kolb *et al.* 2011). These costs can be most effectively reduced with an accurate estimation of the wind loading on a heliostat to maintain the structural integrity during high wind periods while achieving good optical performance during operation of the field (Pfahl *et al.* 2017a). Heliostats are designed to maintain structural stiffness during operation (Figure 1a) at different elevation angles ($\alpha > 0°$) for maximum optical accuracy. Furthermore, they require the structural strength to withstand the maximum loads during high-wind conditions when aligned parallel to the ground ($\alpha = 0°$) in the stow position (Figure 1b). The design wind loads on heliostats are commonly defined using a combination of non-dimensional peak load coefficients that account for the turbulence in the wind and the mean wind speed $\overline{U}_H$ at the elevation axis height (H in Figure 1) above the ground.

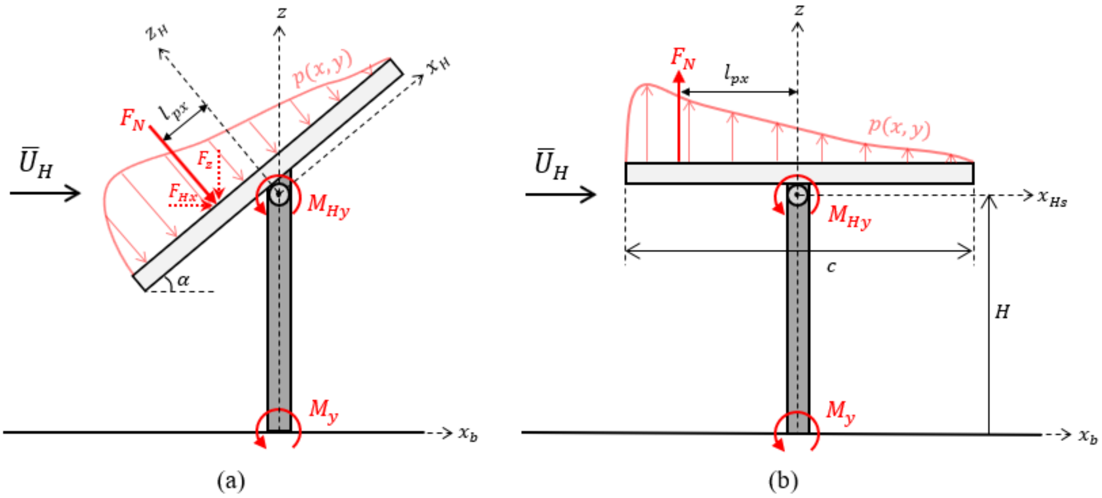

Figure 1. Wind loads on a heliostat due to a non-uniform pressure distribution $p(x, y)$ on the heliostat mirror plane caused by atmospheric turbulence in: (a) operating positions $\alpha > 0°$; (b) stow position $\alpha = 0°$. Reproduced from Emes *et al.* (2019). Positive values of the hinge M_{Hy} and overturning M_y moments are defined by anti-clockwise rotations about the elevation axis y_H and the y-axis of the pylon base y_b, respectively.

The design method for heliostat wind loads (Peterka and Derickson 1992) outlines the critical configurations of the elevation angle α of a square heliostat mirror (chord length c in Figure 1) relative to the horizontal, and the azimuth angle β of the frontal projected heliostat mirror plane relative to the wind direction. Peterka and Derickson (1992) reported the azimuth-elevation configurations (α, β) for the most unfavourable working conditions represented by the maximum values of the peak coefficient of the drag force F_x in the horizontal x direction, lift force F_z in the vertical z direction, hinge moment M_{Hy} about the central elevation axis and overturning moment M_y about the foundation at the base of the steel pedestal of a conventional heliostat. The forces and moments were calculated from high-frequency measurements using strain gauges mounted on a square-facet heliostat model (c = 0.27 m, H = 0.13 m) and in the base of a force balance in a wind tunnel with test section of 2.13 m height, 1.8 m width and 18.29 m length (Peterka *et al.* 1988; Peterka *et al.* 1989). Aerodynamic force and moment coefficients used in heliostat design are therefore commonly calculated using the mean wind speed at the elevation axis height. This follows a quasi-steady approximation that the ratio of the peak and mean forces are proportional to the square of the velocity gust factor defined by the ratio of the 3-second gust wind speed to the mean wind speed (Peterka and Derickson 1992; Mendis *et al.* 2007). The gust factor method can provide reliable estimations of the wind loads on physical structures with standard geometries, such as low-rise buildings with monoslope roofs (ASCE 7-02 2002; AS/NZS 1170.2 2011). However, the aerodynamic mechanisms such as corner vortices generated by buildings have been shown to cause significant differences between the loading on roof-mounted and ground-mounted solar panels (Kopp *et al.* 2012). Furthermore the quasi-steady assumption can under-estimate the load predictions on small physical structures with non-standard geometries, such as the hinge moments on stowed heliostats (Ghanadi *et al.* 2017) due to the large amplitude fluctuations during high-wind events caused by gusts over short time intervals (Durst 1960; Mendis *et al.* 2007).

The design of the load-bearing heliostat components, such as the drive units, pedestal and foundation, requires the distribution of the loads over the mirror to be accurately estimated in operating and stow positions. Eddies embedded in the turbulence lead to fluctuations in the wind velocity and direction, resulting in a non-uniform pressure distribution $p(x, y)$ on the heliostat mirror that varies both temporally and spatially. The temporal distribution of the surface pressure is represented by the mean, root-mean-square (RMS) and peak pressure coefficients, whereas the position of the net force on the heliostat surface due to a non-uniform pressure distribution is given by the centre of pressure. Wind codes and standards for open buildings provide recommendations for the maximum movement of the centre of pressure from the leading edge of the roof surface as a function of the aspect ratio of the roof dimensions and the inclination angle. For example, the centre of pressure distance from the windward edge of a square-cross-section monoslope roof is given in ASCE 7-02 (2002) as 30% of the roof dimension parallel to the wind direction over the 10-20° range of inclination angles, and 40% for a roof inclination angle of 30°. In contrast, EN 1991-1.4 (2010) recommends the maximum movement of the centre of pressure from the centre of a flexible, centrally-supported plate-like structure, such as a signboard, to be less than 25% of the plate chord length (c) normal to the wind direction. Although a square cross-section signboard separated from the ground by a height greater than $c/4$ closely represents the surface geometry of a heliostat, a sign board is a stationary structure with constant inclination angle and therefore has a more limited range of centre of pressure movement compared to a heliostat tracking over a large range of elevation and azimuth angles. There is a linear increase of the centre of pressure toward the leading edge of a thin, square flat plate aligned parallel to the ground ($\alpha = 0°$) with decreasing β from 90° to 0° (Holmes *et al.* 2006). Gong *et al.* (2013) investigated the effect of α and β on the mean, RMS and peak pressure distributions on the heliostat surface. However, the variation of the position of the centre of pressure where the net force acts on the heliostat surface for different azimuth-elevation configurations is not well understood. Hence, the first objective of this paper is to determine the positions of the centre of pressure corresponding to the mean and peak pressure distributions on a heliostat at a range of elevation and azimuth angles.

Peterka and Derickson (1992) derived non-dimensional peak load coefficients to account for the turbulence in the wind from the measured mean wind speed $\overline{U}_H \approx 12.6$ m/s and the turbulence intensity $I_u = \sigma_u/\overline{U}_H = 18\%$, defined as the ratio of the root-mean-square of the fluctuating velocity to the mean wind velocity at the elevation axis height $H = 0.155$ m. The maximum design aerodynamic load coefficients have been reported in scale-model heliostat wind tunnel experiments (Peterka *et al.* 1988; Peterka *et al.* 1989; Peterka and Derickson 1992) over a range of elevation-azimuth configurations in an open country terrain ($z_0 = 0.03$ m) with $I_u = 18\%$ and $G_u = 1.6$ at the heliostat elevation axis height. Turbulence intensities $I_u \geq 10\%$ have been found to significantly influence the peak drag, lift and overturning moment coefficients in operating positions ($\alpha = 15$-90° and $\beta = 0$-180°) by Peterka *et al.* (1988) and Yu *et al.* (2019), and the peak lift and hinge moment coefficients in stow position ($\alpha = 0°$) by Pfahl *et al.* (2015) and Emes *et al.* (2017). Furthermore, the peak drag and lift coefficients on normal and stowed heliostats have been shown to depend on both the turbulence intensity and the longitudinal integral length scales of the energy-containing eddies in the longitudinal and vertical directions, respectively (Jafari *et al.* 2018; Jafari *et al.* 2019a). The aerodynamic coefficients reported by Peterka *et al.* (1989) only specified one worst-case scenario for the peak hinge moment at $\alpha = 30°$ for a range of α between 0° and 180° and $\beta = 0°$. Increasing lift force and pitching moment coefficients have been observed on wings (Holloran and O'Meara 1999) and flat plates (Ortiz *et al.* 2015) as they are positioned closer to the ground. Further knowledge of the effect of changes in β between 0° and 180° on the peak hinge moments, due to the maximum movement of the centre of pressure from the central elevation axis, is critical for the design of the elevation drive to maintain the structural rigidity of the heliostat during operation. Hence, the second objective of this paper is to determine the effect of turbulence intensity on the position of the centre of pressure and the resulting hinge and overturning moment coefficients on heliostats at a range of azimuth and elevation angles.

The influence of the temporal and spatial variations of turbulence in the lowest 10 m of the ABL on the peak load coefficients with changes in aerodynamic surface roughness and heliostat size is an important consideration for the design loads on the drive units, pedestal and foundation. Wind loads on heliostats are highly dependent on the surrounding terrain of a heliostat field, which can be characterised by location, the height above sea level, total area of land, maximum height variations across the terrain and a description of the ground roughness, including any natural topography or structures larger than 2 m in height (AS/NZS 1170.2 2011). Table 1 shows three terrain categories defined by Xu (2013) with the estimated surface roughness parameters z_0 (m) and $\alpha_{\overline{U}}$ for the logarithmic law and power law velocity profiles, respectively. The vertical profiles of turbulence intensities and length scales of the longitudinal u and vertical w velocity components in Figure 2 are taken from ESDU 85020 (2001) using similarity theory formulations of full-scale ABL data as a function of z_0. A flat "open country" terrain is commonly assumed as the surroundings of a heliostat field (Peterka and Derickson 1992; Pfahl *et al.* 2015), where the wind characteristics are derived from the 10-m reference height defined in design wind codes and standards (Holmes 2007). However, the expected loads for the single turbulence condition ($I_u = 18\%$, $G_u = 1.6$) can only be applied to a height of 10 m in an open country terrain with $z_0 = 0.03$ m from ESDU 85020 (2001) full-scale atmospheric boundary layer data in Figure 2(a). The largest heliostats ($A \geq 120$ m^2) currently deployed by Abengoa Solar and Sener are typically designed with $H \leq 6$ m, however smaller heliostats ($A \leq 20$ m^2) developed by eSolar and Brightsource Energy are closer to the ground with $H \leq 3$ m (Téllez *et al.* 2014). Furthermore, heliostat fields are commonly positioned in low-roughness terrains, such as flat deserts and grassy plains (Table 1). The turbulence intensities in a flat desert are approximately 25% smaller at all heights below 10 m compared to an open country terrain, whereas the turbulence length scales increase by 43% at $z = 10$ m and by as much as 82% at $z = 3$ m. Hence, the third objective of this paper is to identify the critical elevation-azimuth configurations of the heliostat corresponding to the hinge and overturning moments in operating positions and determine the maximum operational design wind speeds that allow the operating loads to remain below the ultimate stow design loads.

Table 1. Terrain categories in the ABL (Xu 2013)

Terrain description	z_0 **(m)**	$\alpha_{\bar{U}}$
Open country with isolated trees and buildings	0.03	0.17
Grass and very few trees	0.01	0.15
Flat desert	0.003	0.12

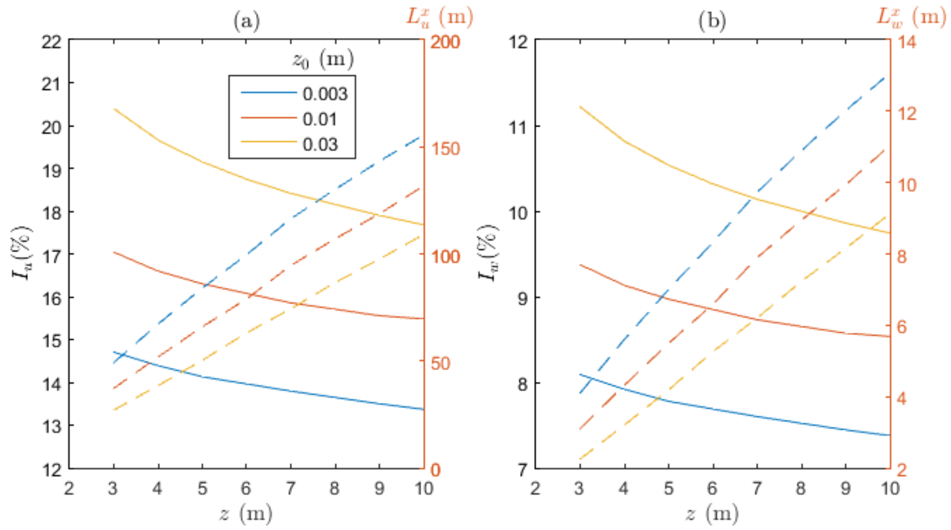

Figure 2. (a) Longitudinal $i = u$, and (b) vertical $i = w$ turbulence intensity I_i and length scale L_i^x profiles from ESDU 85020 (2001) as a function of aerodynamic roughness height z_0 at heights below 10 m where heliostats are positioned in the lower atmospheric surface layer. Solid lines indicate the turbulence intensity profiles and dashed lines indicate the integral length scale profiles.

2. Method

The aerodynamic force and moment coefficients on heliostats are calculated from experimental measurements in a wind tunnel at the University of Adelaide. Surface pressures on an instrumented heliostat (Figure 3) with square cross-section chord length $c = 0.8$ m and forces at the base of the heliostat model with elevation axis height $H = 0.5$ m were sampled at 1 kHz using four three-axis load cells mounted on a force balance. The heliostat facet is attached to a circular hollow section pylon by a hinge pin joint to adjust the elevation angle α in increments of 15° between 0° and 90° and an electronic turntable to adjust the azimuth angle β in increments of 30° between 0° and 180°. The instrumented heliostat is positioned within three simulated part-depth atmospheric boundary layers (ABLs) at longitudinal turbulence intensities of 8%, 13% and 26% at the heliostat elevation axis height $H = 0.5$

m. Further details of the experimental setup of spires and roughness elements for the generation of the ABLs are provided in Yu *et al.* (2019) and Jafari *et al.* (2019a). The experimental devices used for the heliostat surface pressure and force measurements are described in the previously published papers by the authors (Emes *et al.* 2017; Emes *et al.* 2019; Yu *et al.* 2019). The pressure coefficients at each of the 24 tap locations i on the heliostat mirror surface were calculated as:

$$C_{p_i}(t) = \frac{p'(t)}{1/2\rho \overline{U}_H{}^2}\,, \tag{1}$$

where ρ (kg/m^3) is the air density, $\overline{U}_H$ (m/s) is the mean wind speed at the heliostat elevation axis height H, and $p(t) = P_i^f(t) - P_i^b(t)$ (Pa) is the instantaneous differential pressure between the upper and lower surfaces of the heliostat mirror. The net force acting perpendicular to the mirror surface F_N, defined in Figure 1 for operating positions ($\alpha > 0°$) and stow position ($\alpha = 0°$), was calculated in the current study from the area-averaged pressure coefficient in equation 1,

$$F_N = 1/2\rho \overline{U}_H{}^2 \oint -C_{p_i}\, dA\,. \tag{2}$$

Here $A = c \times c$ (m^2) is the area of the heliostat mirror projected onto the x_H-y_H plane in operating positions (Figure 1a) and x_{Hs}-y_{Hs} plane in stow position (Figure 1b). For the derivation of mean and peak wind loads on heliostats (Peterka and Derickson 1992), the net force F_N acting perpendicular to the heliostat mirror at elevation angle α is decomposed into the drag force F_x in the horizontal wind direction and the lift force F_z in the vertical direction as follows:

$$F_x = F_N \sin\alpha\,, \tag{3}$$

$$F_z = F_N \cos\alpha\,. \tag{4}$$

The normal force F_N acts on the heliostat mirror surface at the centre of pressure $l_p = \sqrt{l_{px}{}^2 + l_{py}{}^2}$. Turbulence in the approaching ABL causes a non-uniform differential pressure distribution $p(x, y)$ on the heliostat. The position of the centre of pressure is calculated in the current study as the distance in the longitudinal and lateral directions from the centre of the heliostat surface in Figure 3 by

$$l_{px} = \frac{c}{2} - \frac{\int_0^c xp(x,y)\, dx}{\int_0^c p(x,y)\, dx}\,, \tag{5}$$

$$l_{py} = \frac{c}{2} - \frac{\int_0^c yp(x,y)\, dy}{\int_0^c p(x,y)\, dy}\,. \tag{6}$$

The hinge moment about the elevation y_H axis of the heliostat mirror is

$$M_{Hy} = F_N l_{px} , \tag{7}$$

as the product of the area-averaged net force in equation 2 and the centre of pressure distance l_{px} in equation 5 from the elevation y_H axis in Figure 3b. Similarly, the hinge moment about the x_H axis in the heliostat mirror plane in Figure 3 can be calculated as $M_{Hx} = F_N l_{py}$ using the same coordinate system as in Figure 1 of Peterka and Derickson (1992). The peak forces ($F_{peak} = \bar{F} + 3\sigma_F$) and moments ($M_{peak} = \bar{M} + 3\sigma_M$) are calculated as the sum of the mean values and three times the standard deviation of the fluctuating surface pressure measurements. The three-sigma approach provides peak values with a 99.7% probability of not being exceeded based on extreme value analysis (Simiu and Scanlan 1996). The peak forces derived from the surface pressure measurements are within ±5% of those calculated from the load cell measurements using the same three-sigma approach. Hence, the mean and peak aerodynamic coefficients of the forces and moments are calculated in the current study using the positions of the centre of pressure within the non-uniform pressure distributions, such as those in Figure 5 and Figure 6. Peak coefficients were calculated using the peak force/moment and the mean velocity $\bar{U}_H$ at the heliostat elevation axis (hinge) height H in Figure 1, following the method outlined in Peterka and Derickson (1992) and the equations:

$$c_{Fx} = \frac{F_x}{1/2\rho\bar{U}_H{}^2 A} , \tag{8}$$

$$c_{Fz} = \frac{F_z}{1/2\rho\bar{U}_H{}^2 A} , \tag{9}$$

$$c_{MHx} = \frac{F_N l_{py}}{1/2\rho\bar{U}_H{}^2 Ac} = c_{F_N}\left(l_{py}/c\right) , \tag{10}$$

$$c_{MHy} = \frac{F_N l_{px}}{1/2\rho\bar{U}_H{}^2 Ac} = c_{F_N}\left(l_{px}/c\right) , \tag{11}$$

$$c_{My} = \frac{M_y}{1/2\rho\bar{U}_H{}^2 AH} = c_{MHy}\left(\frac{c}{H}\right) + c_{Fx} . \tag{12}$$

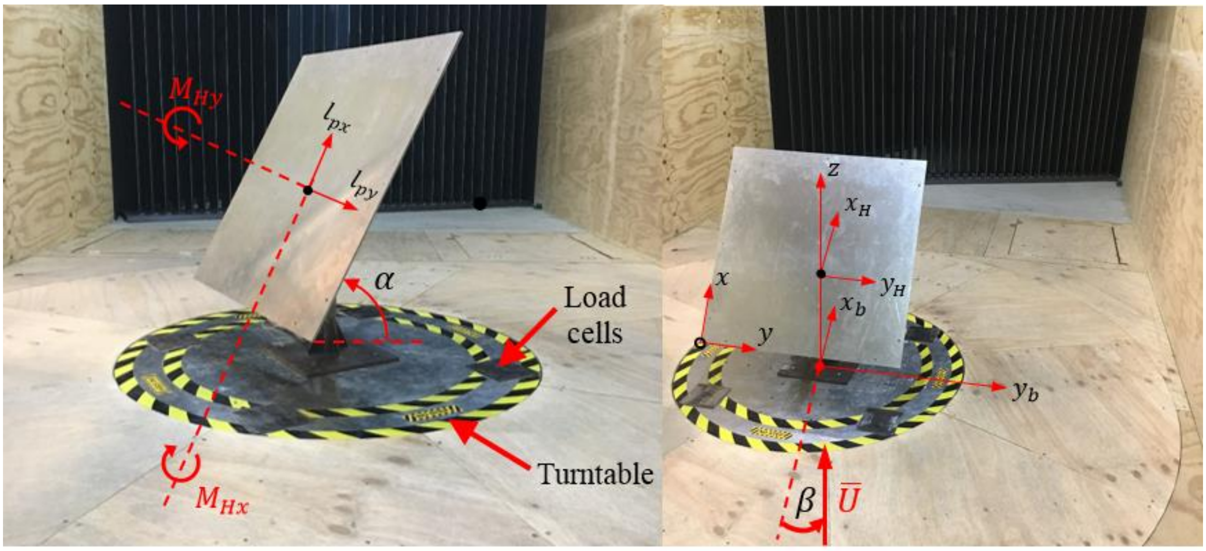

(a) (b)

Figure 3. Experimental setup for measurement of the pressures and forces on a model heliostat at a range of elevation α and azimuth β angles: (a) the centre of pressure $l_p(x,y)$ is defined by the streamwise l_{px} and spanwise l_{py} distances from the centre of the heliostat mirror plane; (b) definition of the coordinate axes (x,y) for the pressure measurements on the heliostat mirror plane, elevation axes (x_H,y_H) at the heliostat hinge height, azimuth z-axis and axes (x_b,y_b) at the base of the heliostat pylon.

3. Results and Discussion

Figure 4 compares the calculated peak aerodynamic force and moment coefficients at $\beta = 0°$ for the two simulated ABLs ($I_u = 13\%$ and 26%) in the current study with those reported by Peterka *et al.* (1989) at $I_u = 14\%$ and 18%. The peak drag (Figure 4a) and lift (Figure 4b) coefficients for operating elevation angles at $I_u = 13\%$ in the current study follow a similar trend to those of Peterka *et al.* (1989) at $I_u = 14\%$. It can be observed that the lift and hinge moment coefficients increase more significantly at smaller elevation angles $\alpha \leq 30°$ and in stow position ($\alpha = 0°$) compared to the study by Peterka *et al.* (1989). Furthermore, the drag and overturning moments at $\alpha \geq 60°$ show a smaller increase with increasing α to 90° in the current study. The largest differences in the peak load coefficients between the two studies at $\alpha = 0°$ and 90° are likely to be caused by variations in the ratio of the turbulence length scales relative to the heliostat chord length (Jafari *et al.* 2018; Jafari *et al.* 2019a). The distribution of turbulence length scales varies significantly with height compared to turbulence intensity in the two part-depth ABL simulations with scale factors of 1:151 and 1:90 in the current study (Jafari *et al.* 2019a). When comparing the peak load coefficients reported by Peterka *et al.* (1989) at $I_u = 18\%$ with the current study at $I_u = 26\%$, the peak drag coefficient at $\alpha = 90°$ increases by 29% from 4.0 to 5.16

and the peak lift coefficient at $\alpha = 30°$ increases by 34% from 2.8 to 3.75. This confirms the approximately linear increases of the peak drag and lift coefficients on heliostats in operating (Peterka *et al.* 1988) and stow (Pfahl *et al.* 2015; Emes *et al.* 2017) positions observed with increasing turbulence at $I_u \geq 10\%$. This is caused by increases in the standard deviation of the fluctuating drag and lift forces, shown by the error bars in Figure 4, with increasing I_u from 13% to 26%. The standard deviation of the drag coefficients increases by a factor of 3 at $\alpha = 0°$ and by up to a factor of 4 at $\alpha = 90°$, whereas those for the lift coefficients increase by factors of between 1.5 at $\alpha = 90°$ and 4.4 at $\alpha = 30°$. It is noted that the standard deviations of the force coefficients at $I_u = 26\%$ are significantly larger than those at $I_u = 13\%$, such that they are similar in magnitude to the mean coefficients. Hence, the peak force and moment coefficients derived for this high-turbulence case are likely to have a larger error margin for estimating the full-scale heliostat loads within the expected range of turbulence conditions (Figure 2) in the lowest 10 m of the ABL.

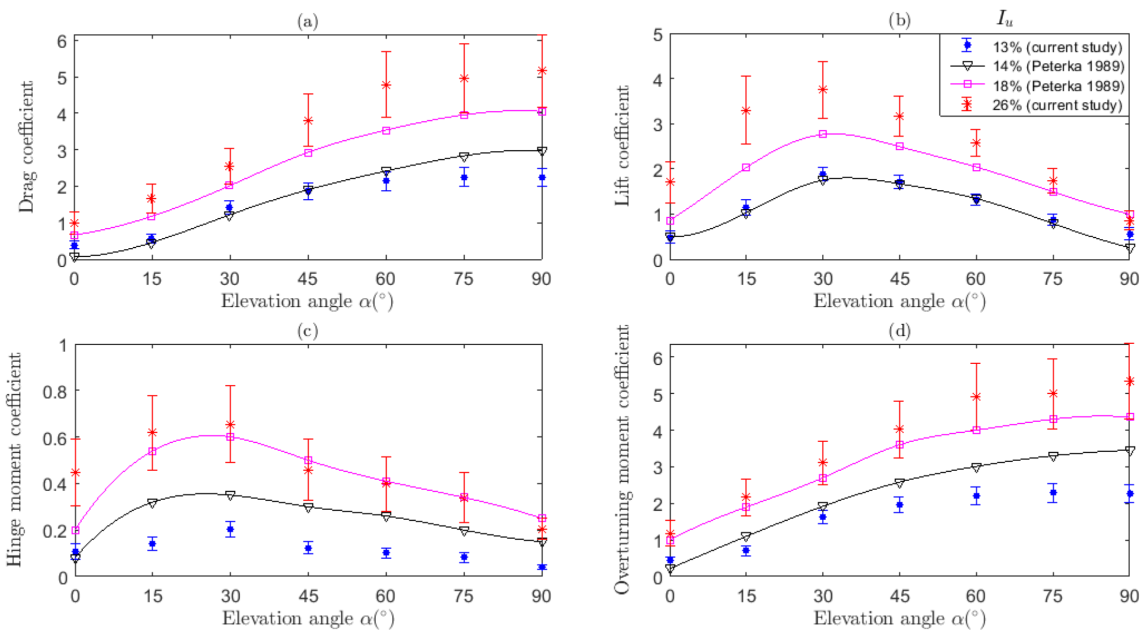

Figure 4. Peak aerodynamic coefficients at azimuth angle $\beta = 0°$ as a function of elevation angle α and turbulence intensity I_u (%) compared with Peterka *et al.* (1989): (a) drag force coefficient c_{FHx}; (b) lift force coefficient c_{Fz}; (c) hinge moment c_{MHy}; (d) overturning moment c_{My}. Error bars indicate one standard deviation of the coefficients from the mean values.

3.1. Heliostat Pressure Distributions

Figure 5 and Figure 6 show the mean and standard deviation pressure coefficient distributions, respectively, on the heliostat surface at different elevation α and azimuth β angles within the simulated

ABL at a turbulence intensity $I_u = 13\%$. The region of high suctions on the heliostat surface at $\beta = 0°$ with mean $C_p > 2$ and standard deviation $C_p > 0.4$ moves towards the leading edge ($x = 0$ m) with decreasing α from 60° to 15°. The maximum values of the peak pressure coefficients calculated following the three-sigma approach at $\alpha = 30°$ in the current study ($C_p = 2.92$) are consistent with peak C_p values of 3.4 near the leading edge and 2.62 near the central elevation axis in the distribution of Pfahl *et al.* (2011) at $\alpha = 30°$ and $\beta = 0°$. A similar trend to Gong *et al.* (2013) is found that the high-magnitude region of the mean pressure coefficient distribution in Figure 5 is concentrated near the windward edge of the heliostat with the mean C_p at $\alpha = 60°$ increasing to 2.1 at $\beta = 0°$, 2.7 at $\beta = 60°$, -1.8 at $\beta = 150°$ and -2.02 at $\beta = 180°$. The maximum values of mean C_p at $\alpha = 60°$ in the current study are larger than the mean $C_p = \pm 1.2$ at $\beta = 0°$ and 180° and $C_p = \pm 1.5$ at $\beta = 60°$ and 150° in Gong *et al.* (2013). The reason for the variability in the pressure coefficients of the current study, Pfahl *et al.* (2011) and Gong *et al.* (2013) is likely to be the differences in the heliostat model size, turbulence intensities and length scales in the simulated ABLs. Although the longitudinal turbulence intensities are similar in these studies, differences in the ratio of the turbulence length scales and the heliostat model dimensions and the consequent mismatch of the turbulence spectra can lead to variations in the unsteady loads measured on the models (Jafari *et al.* 2019b). The standard deviation pressure coefficients in Figure 6 show that the large magnitude pressure fluctuations ($C_{p,std} > 0.4$) extend further from the windward edge towards the centre of the heliostat than the mean pressure coefficients. For example, the position of the high-magnitude fluctuating pressures extends to 0.2 m downstream of the windward edge in the x-direction at $\alpha = 15°$, compared to a maximum lateral distance of 0.13 m from the side edge of the heliostat ($y = 0.8$ m) at $\alpha = 30°$. In contrast for stow position ($\alpha = 0°$), the mean pressure coefficients are smaller in magnitude but the high-pressure region spans a greater portion of the windward edge of the heliostat. This corresponds to the maximum movement of the centre of pressure towards the windward edge at $\beta = 0°$ and 180° with highly correlated pressures across the width of the stowed heliostat surface. Further, the magnitudes of the mean and standard deviation pressure coefficients in stow and operating positions indicate that the maximum forces on the heliostat structure occur when the wind is perpendicular to the heliostat surface at $\beta = 0°$ and 180°. There is a change of sign of the mean pressure coefficients on operating heliostats as β increases beyond 90°, such that the wind approaches the inclined heliostat from behind and the differential pressure between the upper and lower surfaces becomes negative. The high-pressure regions from separation of the approaching turbulent flow over the maximum width of the windward edge causes the largest variation in pressure along the mirror in the x-direction. The maximum hinge moment is thus likely to be characterised by strong suctions near the leading edge at $\alpha = 15°$ and 30°, as the standard deviation pressure coefficients become more highly correlated across the span of the heliostat at $\beta = 0°$ and 180°. This suggests that the distribution of the turbulent pressure fluctuations indicated by the movement of the centre of pressure is critical for the peak hinge moments on heliostats at smaller elevation angles $\alpha \leq 30°$. The peak hinge moment is decisive for the design wind loads on the elevation drive of a conventional pedestal-mounted heliostat, particularly at smaller elevation angles and in stow position. Hence, the spanwise-averaged distribution of pressure in the along-wind x-direction of the heliostat surface and the position of the centre of pressure where the net force acts corresponding to the peak hinge moment on the heliostat should be considered for design loads.

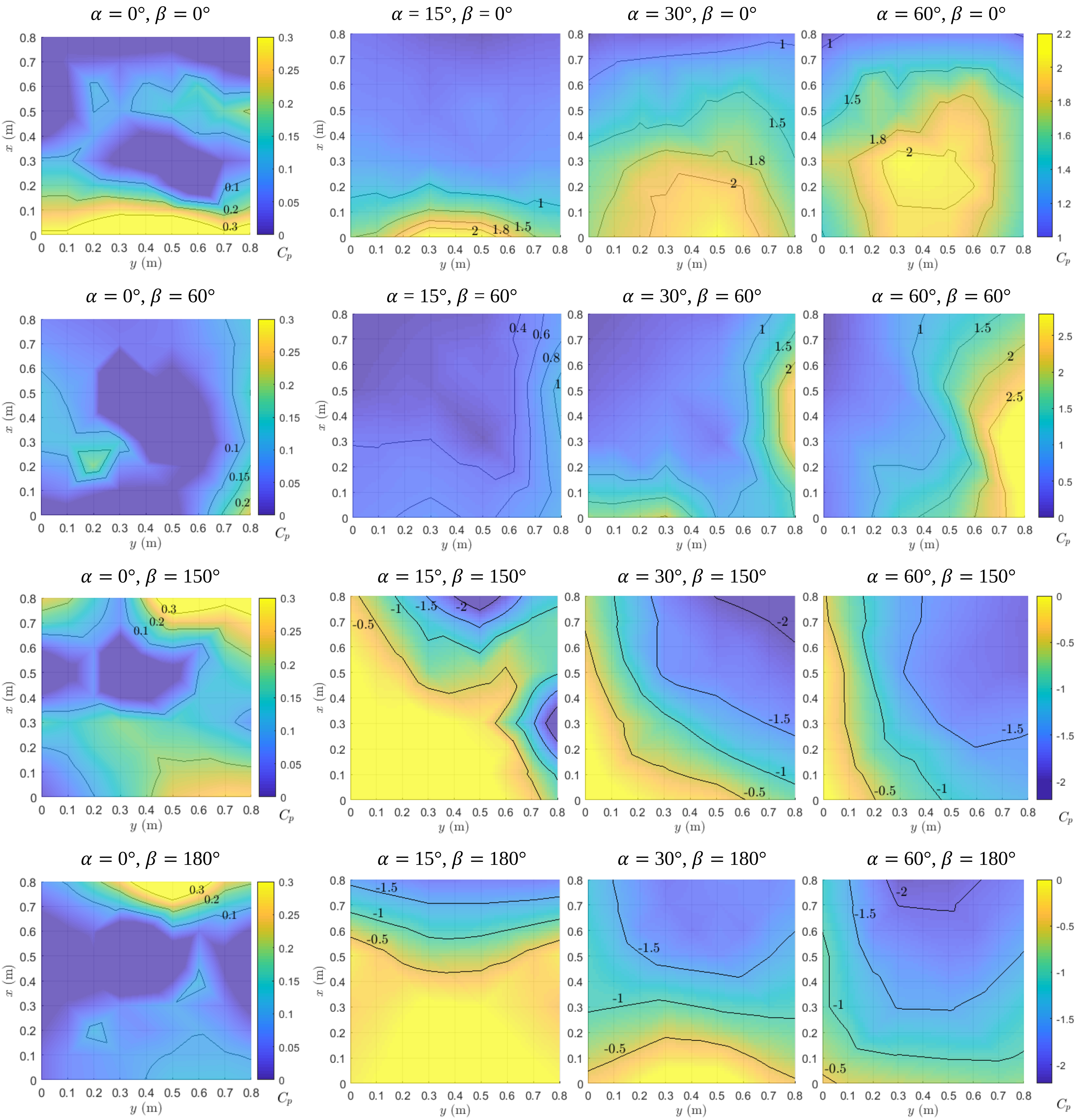

Figure 5. Surface contour distributions of the mean pressure coefficients on the heliostat surface at different elevation α and azimuth β angles within a simulated ABL at a turbulence intensity $I_u = 13\%$ at the heliostat elevation axis height. The leading edge at $\beta = 0°$ corresponds to $x = 0$ m. The black lines indicate constant C_p values and the coloured bar on the right side of each row (at constant β) shows the range of mean pressure coefficients.

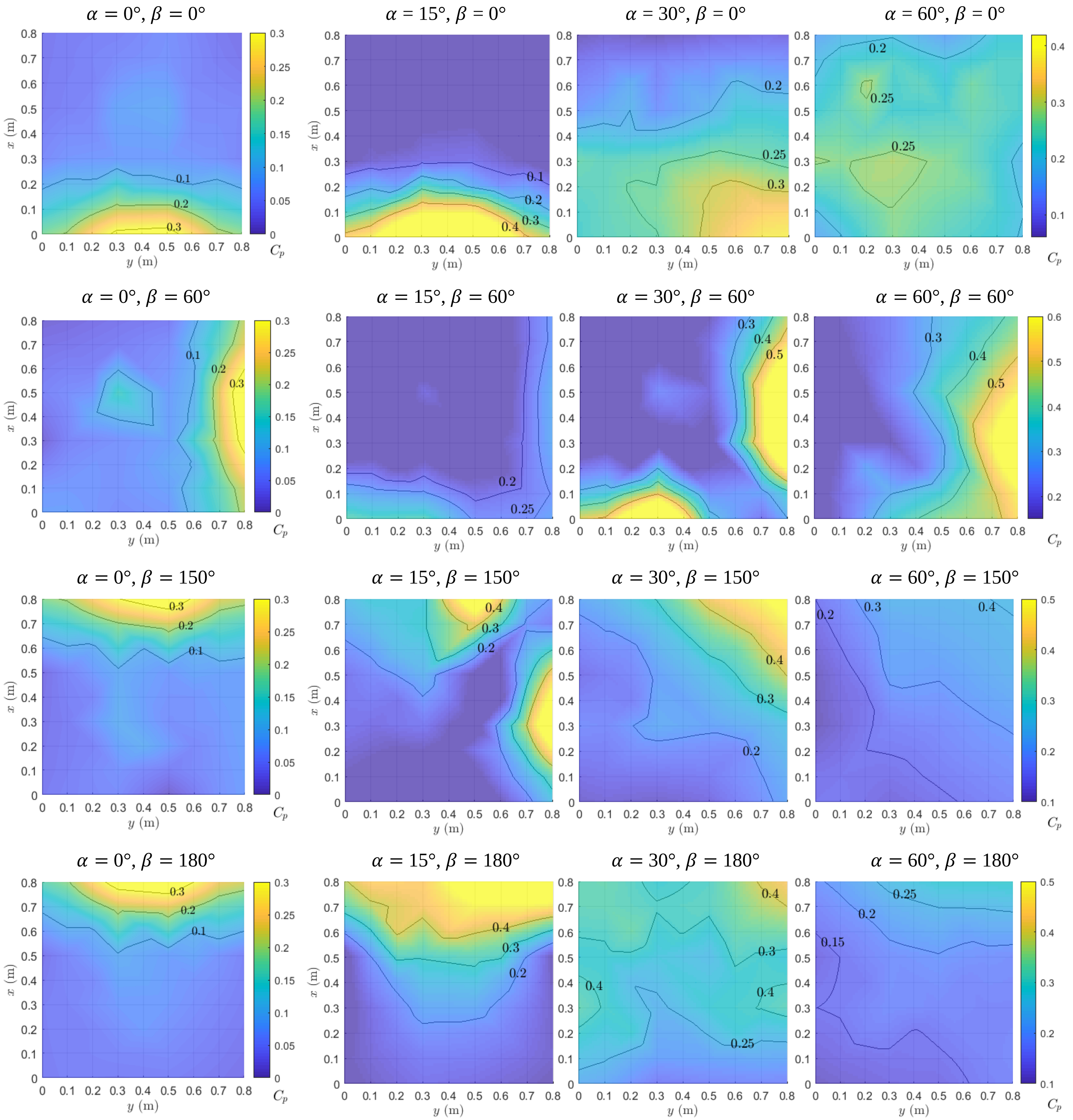

Figure 6. Surface contour distributions of the standard deviation pressure coefficients on the heliostat surface at different elevation α and azimuth β angles within a simulated ABL at a turbulence intensity $I_u = 13\%$ at the heliostat elevation axis height. The black lines indicate constant C_p values and the coloured bar on the right side of each row (at constant β) shows the range of the standard deviation pressure coefficients.

Figure 7 shows the average position of the centre of pressure l_{px} from the central elevation axis in the longitudinal direction x on the heliostat surface in Figure 1(a), as a non-dimensional ratio of the chord length of the heliostat at different elevation and azimuth angles. The average distance where the net force acts on the heliostat surface increases with decreasing elevation angle α from 90° to 15° for all of the azimuth angles β. The largest positive values of l_{px}/c from the movement of the normal force towards the trailing edge of the heliostat occur at $\beta = 180°$, whereas the largest negative values of l_{px}/c at $\beta = 0°$ correspond to the movement of the normal force towards the heliostat's leading edge in Figure 3. The smallest values of $|l_{px}/c| \leq 0.03$ occur at all elevation angles when the wind approaches the heliostat at $\beta = 90°$ and all azimuth angles in stow position at $\alpha = 0°$ for $|l_{px}/c| \leq 0.11$. The profiles of l_{px}/c are similar at $I_u = 13\%$ (Figure 7a) and $I_u = 26\%$ (Figure 7b), which indicates that the effect of turbulence intensity is not significant on the mean pressure distribution on the heliostat. The average position of the centre of pressure $|l_{px}/c| \geq 0.1$ is most significant at the smaller operating elevation angles $\alpha = 15°$ and 30° and for wind approaching the windward ($\beta = 0°$) or leeward ($\beta = 180°$) edges of the heliostat surface. The maximum l_{px}/c occurs at $\alpha = 15°$ for these two critical azimuth angles, where the absolute magnitude of l_{px}/c at $\beta = 180°$ is approximately double that at $\beta = 0°$ for both turbulence intensities in Figure 7(a) and Figure 7(b). The largest movement of the time-averaged centre of pressure l_{px}/c toward the leading edge at $\alpha = 15°$ is due to the increased pressure on the lower surface of the heliostat caused by the ground not allowing the flow to expand as it would without the presence of a lower boundary. This is analogous to the "ground effect" observed on wings (Holloran and O'Meara 1999) and flat plates (Ortiz *et al.* 2015) at small angles of attack near the ground at $H/c \leq 0.5$. The small difference between the mean l_{px}/c in stow position ($\alpha = 0°$) at $\beta = 0°$ and 180° is likely to be due to the small average differential pressures measured for this case that are close to the maximum error of the pressure sensors. The heliostat surface is supported by a hinge pin joint and telescopic pylon in the absence of a torque tube in the heliostat model in the current study, as shown in Figure 8. The decreased magnitudes of the mean pressure coefficients (Figure 5) at $\beta = 180°$ compared to $\beta = 0°$ on the heliostat in operating positions ($15° \leq \alpha \leq 60°$) confirms the finding by Gong *et al.* (2013). Furthermore, the differences in the mean pressure distributions at these two azimuth angles leads to an increased movement of the centre of pressure (Figure 7) from the central elevation axis at $\beta = 180°$ caused by flow separation generated by the rectangular prism shape of the hinge joint protruding from the back of the heliostat surface in Figure 8(a). Hence, wind approaching the back of the heliostat ($\beta = 180°$) should be considered in addition to the front of the heliostat ($\beta = 0°$) for the critical mean pressure distributions on operating heliostats, such as at $\alpha = 15°$, that lead to the largest movement of the time-averaged net force from the central elevation axis.

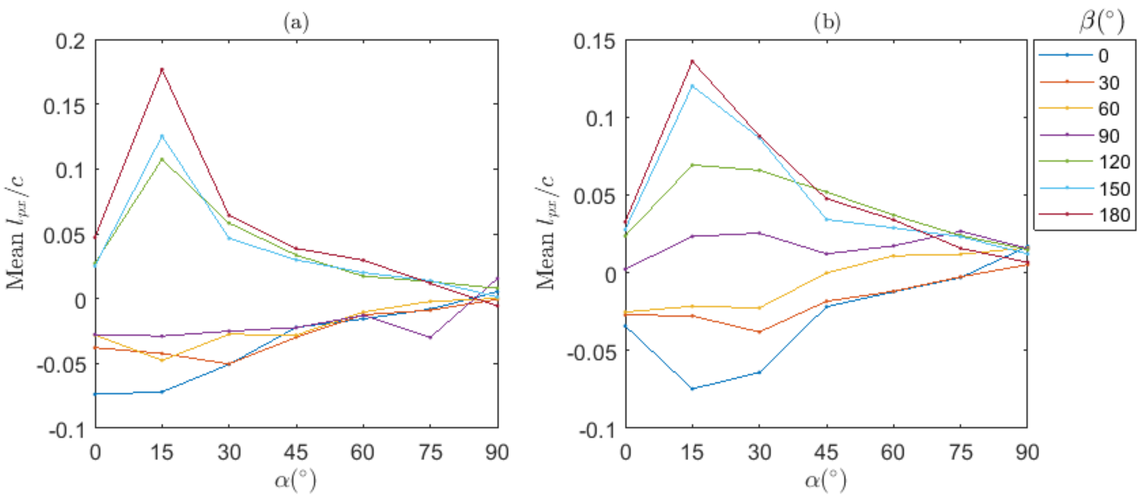

Figure 7. Average position of the centre of pressure l_{px}/c in the streamwise x direction from the central elevation y_H axis of a heliostat at different elevation and azimuth angles: (a) $I_u = 13\%$; (b) $I_u = 26\%$.

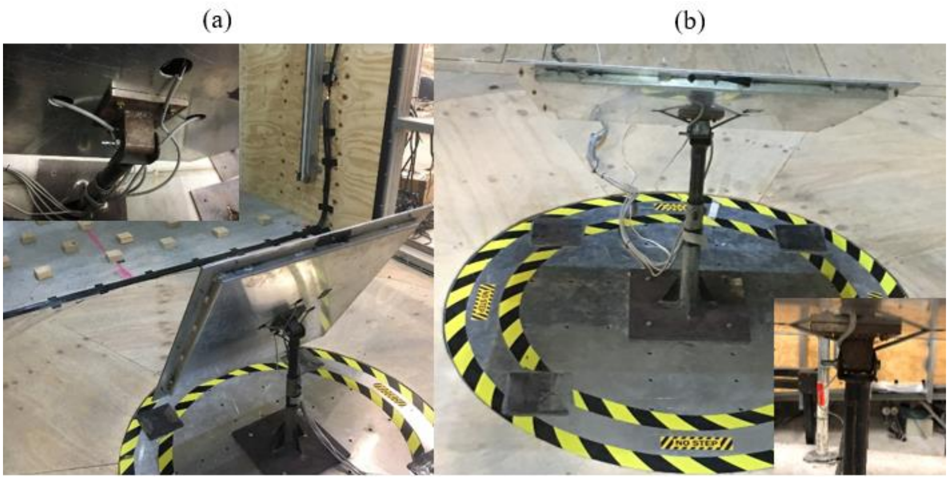

Figure 8. Heliostat model and inset photos of the hinge pin joint and telescopic pylon design: (a) back view of the model in a high-elevation ($\alpha = 75°, \beta = 0°$) operating position; (b) front view of the model in stow ($\alpha = 0°, \beta = 180°$) position.

Figure 9 shows the peak movement of the centre of pressure l_{px} in the longitudinal direction from the central elevation y_H axis of the heliostat, calculated following the three-sigma approximation as a non-dimensional ratio of the chord length of the heliostat at different elevation and azimuth angles. Similar to the mean l_{px}/c in Figure 7, the peak l_{px}/c decreases in magnitude with increasing α to approximately zero at $\alpha = 90°$. The maximum absolute values of the peak l_{px}/c of 0.3-0.4 occur in stow position ($\alpha = 0°$) at all azimuth angles β investigated. The magnitudes of $l_{px}/c \approx 0.3$ and their variation with β at $\alpha = 0°$ in stow position are consistent with experimental data reported by Holmes *et al.* (2006), however at $\alpha \leq 30°$ the maximum movement of l_{px}/c is larger at $\beta = 180°$ due to the increased build-up of pressure near the trailing edge ($x = 0.8$ m in Figure 5 and Figure 6) of the lower surface of the heliostat. The peak l_{px}/c is also less sensitive than the mean l_{px}/c (Figure 7) to changes in β at all of the elevation angles tested. The turbulence intensity of the simulated ABL has a more significant impact on the peak l_{px}/c when comparing Figure 9(a) and Figure 9(b). There is a more pronounced increase in l_{px}/c with decreasing α at the higher turbulence intensity $I_u = 26\%$ in Figure 9(b). For example, $l_{px}/c = 0.07$ and 0.16 at $\alpha = 60°$ and $\alpha = 30°$ for $\beta = 180°$ at $I_u = 26\%$, compared to $l_{px}/c = 0.05$ and 0.11 for the same elevation-azimuth configurations at the lower turbulence intensity $I_u = 13\%$. Hence, the maximum movement of the centre of pressure from the central elevation axis is highly sensitive to the turbulence of the approaching flow and less affected by changes in the azimuth angle from the maximum cases at $\beta = 0°$ and $\beta = 180°$.

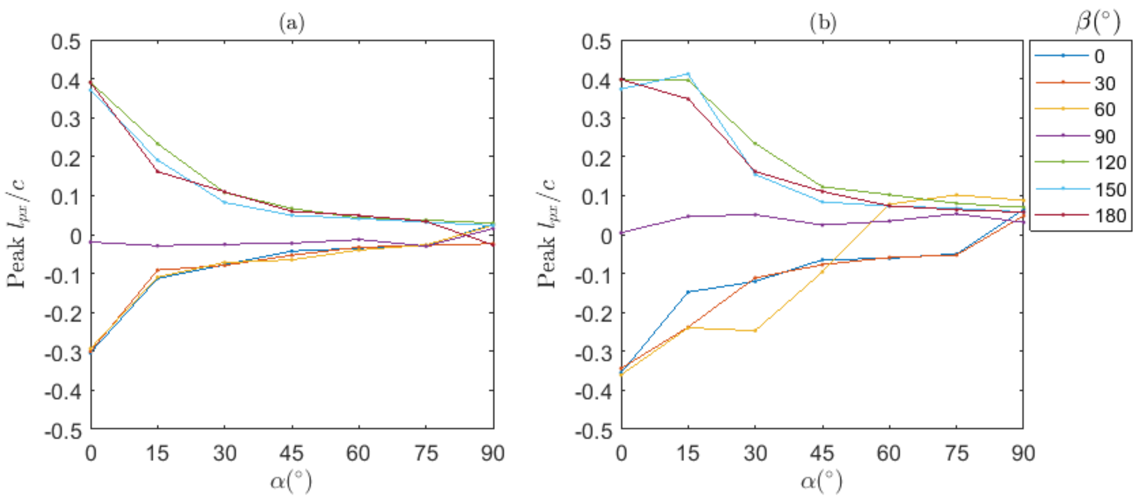

Figure 9. Peak position of the centre of pressure from the central elevation y_H axis of a heliostat at different elevation and azimuth angles: (a) l_{px}/c at $I_u = 13\%$; (b) l_{px}/c at $I_u = 26\%$.

Figure 10 presents the peak pressure coefficients, calculated from the sum of the mean and three times the standard deviation of the spanwise-averaged pressure coefficients in Figure 5 and Figure 6, as a function of the longitudinal distance x/c on the heliostat surface at elevation and azimuth angles corresponding to the maximum l_{px}/c in Figure 9. Comparison of the peak C_p profiles at $\beta = 0°$ indicates that the peak normal force acting toward the upward-facing heliostat surface, calculated from the integral of the C_p profile as a function of x in equation 2, increases to larger positive values with increasing α from 0° to 30°. Similarly, the peak normal force acting toward the downward-facing heliostat surface at $\beta = 180°$ becomes increasingly negative. The peak normal force in Figure 10(a) at $\beta = 180°$ is 48%, 1% and 10% smaller than the corresponding force at $\beta = 0°$ for $\alpha = 0°$, 15° and 30°, respectively. With increasing turbulence in Figure 10(b) the differences in the peak normal force between $\beta = 0°$ and 180° at these elevation angles are 80%, 45% and 29%, respectively. However, the smaller absolute magnitude of the normal force at $\beta = 180°$ is accompanied by a larger movement of the centre of pressure l_{px}/c than for $\beta = 0°$ in Figure 9. This can be observed at $\beta = 0°$ and 180° in Figure 10(a) and Figure 10(b) by the larger increase in the absolute magnitude of C_p near the leading edge at $\alpha = 15°$ compared to $\alpha = 30°$. The larger increase of l_{px}/c near the leading edge at $\alpha = 15°$ contributes to a larger moment arm for the hinge moment M_{Hy} about the central elevation y_H axis of the heliostat.

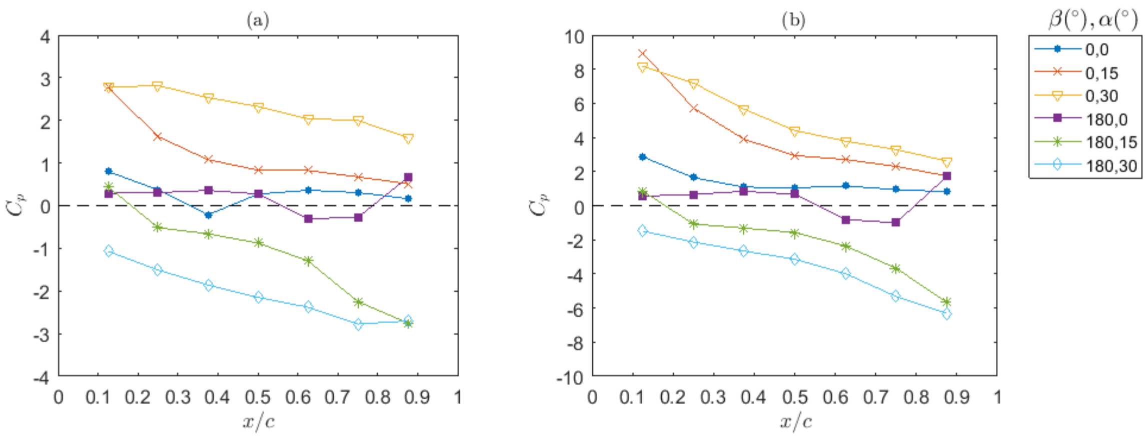

Figure 10. Spanwise-averaged profiles of the peak pressure coefficients in the longitudinal x-direction of the heliostat surface at elevation-azimuth configurations corresponding to the maximum movement of the centre of pressure at: (a) $I_u = 13\%$; (b) $I_u = 26\%$. The leading edge of the heliostat for azimuth angles of $\beta = 0°$ and 180° is at $x/c = 0$ and 1, respectively.

Figure 11 shows the peak movement of the centre of pressure l_{px}/c from the central elevation y_H axis of the heliostat ($c = 0.8$ m) at $\beta = 0°$ as a function of longitudinal turbulence intensity I_u and integral length scale L_u^x measured at the heliostat elevation axis height ($H = 0.5$ m). The effect of increasing longitudinal turbulence in the approaching boundary layer flow has the largest influence on the fluctuating component of l_{px}/c in stow position ($\alpha = 0°$), as indicated by the error bars representing one standard deviation from the mean l_{px}/c. The peak l_{px}/c increases by 38% from 0.22 to 0.3 for an increase in I_u from 8% to 13%, and by 20% from 0.3 to 0.36 with an increase in I_u from 13% to 26%. The large error bars of the peak l_{px}/c at $\alpha = 0°$ are caused by the unsteady pressure fluctuations with near-zero mean values in stow that are highly concentrated near the leading edge of the heliostat surface. Hence, the uncertainty of the calculated peak l_{px}/c in stow is relatively large compared to the other elevation angles tested in the current study. Nevertheless, the maximum movement of l_{px}/c toward the leading edge at $\alpha = 0°$ in the current study is consistent with $l_{px}/c = 0.3$ reported by Holmes *et al.* (2006) in experimental measurements on a thin flat plate aligned parallel to a longitudinal flow with an unknown turbulence intensity. As the elevation angle of the heliostat increases in operating positions, the peak l_{px}/c decreases significantly in magnitude and varies linearly with I_u and L_u^x. For instance, the peak l_{px}/c increases to a maximum of 0.15 at $\alpha = 15°$, 0.12 at $\alpha = 30°$ and 0.06 at $\alpha = 90°$. At constant I_u and L_u^x in Figure 11, the values of peak l_{px}/c on the heliostat at $\alpha = 15°$ and 30° increase due to the build-up of uniform pressure on the lower surface from the flow acceleration in the gap between the windward heliostat edge and the ground. The "ground effect" causes an increased normal force and centre of pressure movement on the heliostat with increasing turbulence compared to that on a square cross-section (length c × depth c) monoslope roof with mid-roof height $H > 18$ m in ASCE 7-02 (2002). The aerodynamic effects of corner vortices generated by flow separation at the building edges also cause differences in the position of the centre of pressure in the load distributions on ground-mounted and roof-mounted solar panels (Kopp *et al.* 2012). At the elevation angles $\alpha > 0°$ of operating heliostats, the position of the centre of pressure shows an approximately linear increase with the spatial and temporal variations of turbulence at heights below 10 m is the maximum hinge moments on heliostats. However, it is suggested that the effect of changes in L_u^x/c on l_p/c should be investigated in future studies, considering the large range of heliostat sizes that are currently deployed in operational PT plants and under construction in active projects.

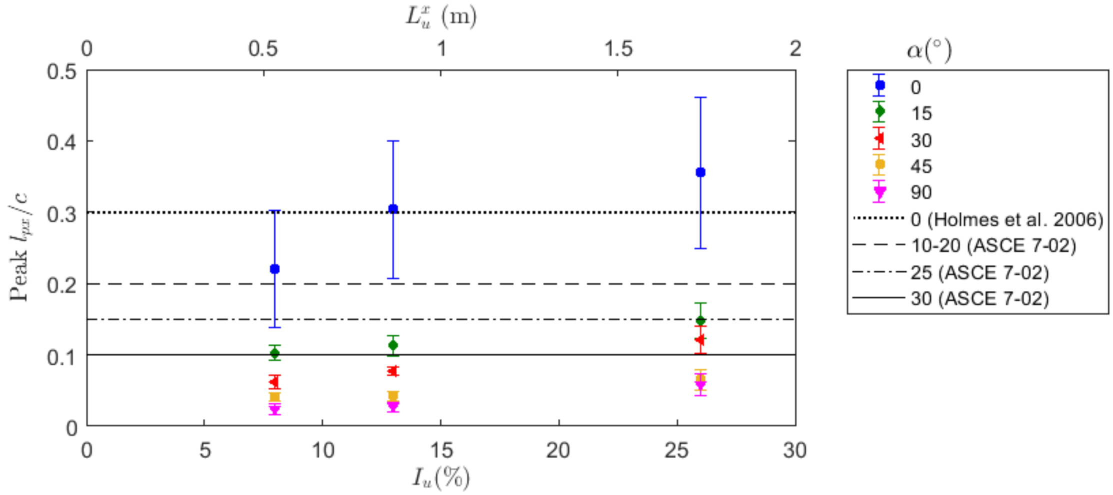

Figure 11. Effect of longitudinal turbulence intensity I_u and length scale L_u^x on the peak movement of the non-dimensional centre of pressure l_{px}/c from the central elevation y_H axis of a heliostat with chord length c at different elevation angles for $\beta = 0°$. Values of l_{px}/c are compared with a square flat plate (Holmes *et al.* 2006) and a square cross-section monoslope roof with mid-roof height $H > 18$ m (ASCE 7-02 2002). The error bars represent one standard deviation of the non-dimensional centre of pressure distance from the mean values.

3.2. Heliostat Hinge and Overturning Moment Coefficients

Figure 12 shows the mean and peak hinge moment coefficients c_{MHy}, calculated using equation 11 as the product of the normal force coefficient and the non-dimensional distance to the centre of pressure, as a function of the elevation and azimuth angles for the two turbulence intensities investigated in the current study. For the lower turbulence case at $I_u = 13\%$, the peak positive (anti-clockwise direction in Figure 1a) c_{MHy} of 0.20 occurs at $\alpha = 30°$ and $\beta = 30°$, whereas the peak negative (clockwise direction in Figure 1a) c_{MHy} of -0.22 corresponds to the heliostat configuration of $\alpha = 30°$ and $\beta = 180°$. In comparison at $I_u = 26\%$, the peak positive c_{MHy} is 0.65 at $\alpha = 30°$ and $\beta = 0°$ and the peak negative c_{MHy} is -0.76 at $\alpha = 15°$ and $\beta = 180°$. Hence, the mean c_{MHy} are most sensitive to the elevation-azimuth configuration of the heliostat and the area-averaged normal force on the heliostat surface. In contrast, the peak c_{MHy} about the central elevation y_H-axis are highly dependent on the maximum distance to the centre of pressure l_{px}/c (Figure 9) within the non-uniform pressure distribution resulting from the turbulent velocity fluctuations in the ABL. The maximum values of the c_{MHy} within a turbulent ABL typically correspond to small elevation angles $\alpha =$ 15-30° with wind approaching the front ($\beta =$

0°) or back ($\beta = 180°$) of the heliostat, whereas Peterka *et al.* (1989) only reported the absolute values of the maximum hinge moment and lift force coefficients at $\alpha = 30°$ and $\beta = 0°$. Despite a smaller normal (and lift) force on the heliostat at $\beta = 180°$, the maximum positive movement of the l_{px}/c at $\alpha = 15°$ in the highly turbulent flow at $I_u = 26\%$ is larger than at $\beta = 0°$ due to the increasing pressure near the windward edge of the lower heliostat surface. The maximum absolute value of the hinge moment coefficient therefore may not occur at the same azimuth-elevation heliostat configuration as the maximum lift force coefficient, as suggested by Peterka and Derickson (1992). Hence, the effect of turbulence intensity on the movement of the centre of pressure, particularly for cases of wind approaching the front ($\beta = 0°$) and leeward ($\beta = 180°$) sides of the heliostat at $\alpha \leq 30°$, should be considered for the design operating loads on the elevation drive of a conventional pedestal-mounted heliostat.

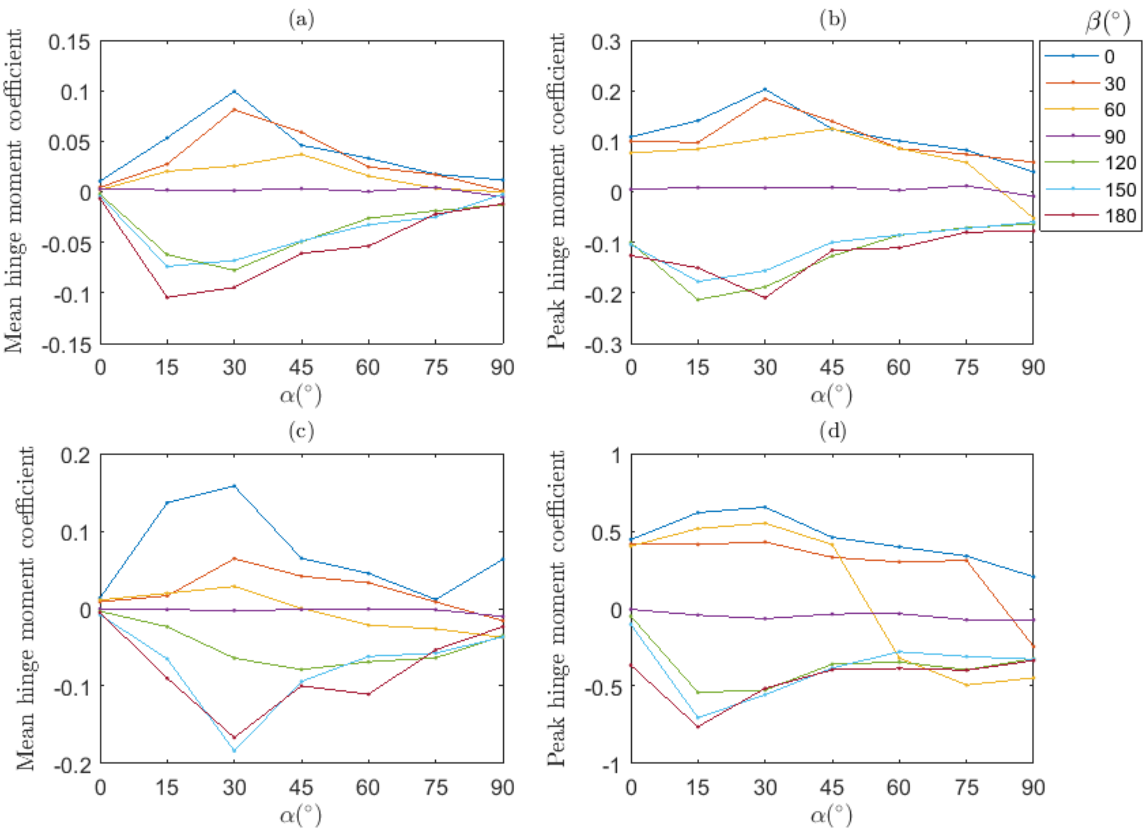

Figure 12. Hinge moment coefficients c_{MHy} about the central elevation axis of the heliostat at different elevation and azimuth angles: (a) Mean at $I_u = 13\%$; (b) Peak at $I_u = 13\%$; (c) Mean at $I_u = 26\%$; (d) Peak at $I_u = 26\%$.

Figure 13 shows the peak overturning moment coefficient c_{My} about the base of the heliostat as a function of elevation and azimuth angles for the two simulated ABLs in the current study. The peak

c_{My} increases with increasing elevation angle from stow ($\alpha = 0°$) to maximum values at $\alpha = 90°$ for wind approaching the front ($\beta = 0°$) or back ($\beta = 180°$) of the heliostat. Similarly to the peak c_{MHy} in Figure 12, the peak c_{My} is relatively independent of β and lowest in magnitude at $\beta = 90°$ due to the small drag force acting on the minimum projected area of the thin heliostat facet. The effect of β increasing from 0° to 60° corresponds to a maximum reduction in peak c_{My} on a normal heliostat ($\alpha = 90°$) of 34% and 50% at $I_u = 13\%$ and 26%, respectively. The increase of c_{My} with increasing α and decreasing β is largely caused by the strong correlation of the overturning moment to the drag force on operating heliostats. However, the effect of β is attenuated in stow position at $\alpha = 0°$ due to the reduced influence of drag and the increasing impact of the hinge moment. Hence, the overturning moment coefficients on a heliostat are largely dependent on azimuth-elevation configuration of the heliostat due to their dependence on the drag force increasing with an increase in the projected frontal area of the heliostat to the wind. In contrast in stow position, the overturning moment coefficient is independent of azimuth angle and is more closely correlated to the hinge moment resulting from the movement of the centre of pressure within the unsteady pressure distribution.

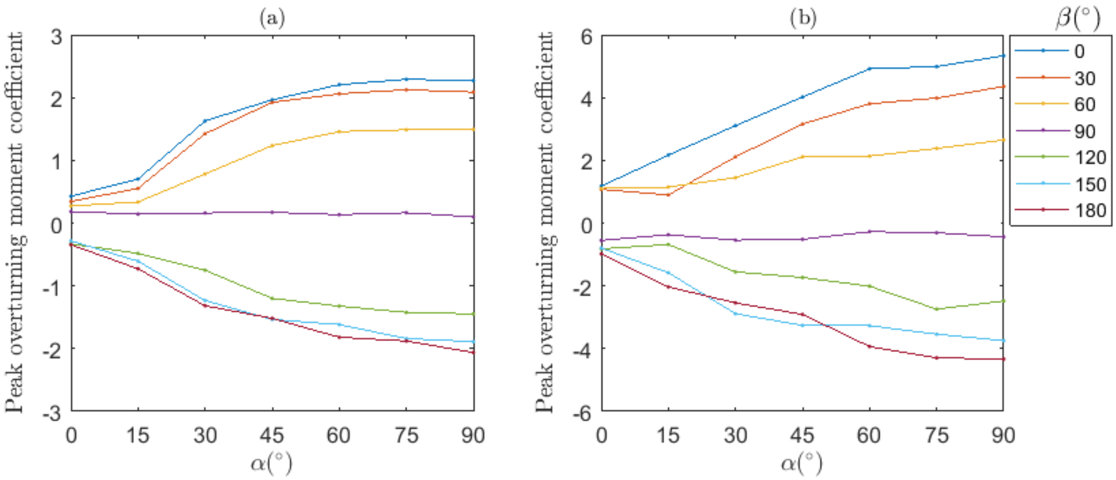

Figure 13. Peak overturning moment coefficients c_{My} as a function of elevation angle α and azimuth angle β at: (a) $I_u = 13\%$; (b) $I_u = 26\%$.

Table 2 compares the critical heliostat α-β configurations as a function of turbulence intensity corresponding to the maximum and minimum moment coefficients with the peak coefficients reported by Peterka *et al.* (1989). The minimum (negative) hinge moment coefficients c_{MHy} are 5% and 17% larger in magnitude than the maximum (positive) c_{MHy} at $I_u = 13\%$ and 26%, respectively. Further, the absolute maximum c_{MHy} values occur at the heliostat configurations of $\beta = 180°$ and $\alpha = 30°$ at $I_u = 13\%$, and for $\beta = 180°$ and $\alpha = 15°$ at $I_u = 26\%$. This result suggests that the unfavourable working condition of $\alpha = 30°$ and $\beta = 0°$ found by Peterka *et al.* (1989) may not correspond to the maximum operating hinge moment for all turbulence conditions. Hence, wind approaching the leeward side of the downward-facing heliostat surface at $\beta = 180°$ in the operating range $\alpha = 15$-$30°$ should be considered for the critical hinge moment cases. The critical heliostat configuration of $\alpha = 90°$ and $\beta = 0°$ for the peak overturning moment coefficient c_{My} is consistent with the finding of Peterka *et al.* (1989). This confirms that critical load cases for c_{My} are not strongly correlated to the hinge moment resulting from the non-uniform pressure distribution, but are largely dependent on the maximum drag force with the maximum frontal projected area of the heliostat surface to the wind.

Table 2. Critical heliostat configurations for the peak positive (anti-clockwise direction of rotation in Figure 1a) and negative (clockwise direction of rotation in Figure 1a) moment coefficients as a function of turbulence intensity, compared with the absolute maximum coefficients reported by Peterka *et al.* (1989).

Load coefficient	**Heliostat configuration**		**Current study**		**Peterka *et al.* (1989)**	
	α (°)	β (°)	13%	26%	14%	18%
Hinge moment $\boldsymbol{c_{MHy}}$	30	0	0.20	0.65	0.35	0.60
	30,15	180	-0.21	-0.76		
Overturning moment $\boldsymbol{c_{My}}$	90	0	2.29	5.33	3.45	4.35
	90	180	-2.01	-4.21		

3.3. Effect of Design Wind Speed on Operating Heliostat Loads

This section presents the ratios of the maximum operating and stow hinge and overturning moments as a case study on a 6 m × 6 m heliostat with $H/c = 0.5$ as a function of elevation angle and the operating design gust wind speed ($\widehat{U}_{op}$). The maximum operating loads, calculated at selected gust wind speeds between 10 m/s and 30 m/s for different elevation angles at $\beta = 0°$, are normalised with respect to a constant maximum stow load for an assumed ultimate design condition $\widehat{U}_{st} = 40$ m/s gust wind speed at a 10 m height. The survival design wind speed for heliostats in stow position is 40 m/s at a 10-m height based on a 100-year mean recurrence interval (Murphy 1980). This is equivalent to the 3-second gust wind speed specified at the 10 m height in design wind codes and standards for buildings and other physical structures, such as in exposed open terrains within Region A of AS/NZS 1170.2 (2011). The peak operating and stow moments in this section are calculated using the peak aerodynamic coefficients at $\beta = 0°$ in Section 3.2 and equations 11-12. The mean wind speed at the elevation axis height $H = 3$ m is calculated from the 10-m height gust wind speed using the gust factor $G_u = U_{des}/\overline{U}_H$ and velocity profile exponent calculated in the wind tunnel for the two turbulence cases: a moderate turbulence intensity $I_u = 13\%$ corresponding to a flat desert terrain in Table 1 and Figure 2 with power law velocity profile exponent $\alpha_{\overline{U}} = 0.12$ and gust factor $G_u = 1.44$, and a high turbulence intensity $I_u = 26\%$ corresponding to a suburban terrain with $\alpha_{\overline{U}} = 0.2$ and $G_u = 1.70$.

Figure 14 shows that the maximum operational hinge moment on the 36 m^2 heliostat at $\alpha = 30°$ exceeds the stow hinge moment by 5% in the desert terrain with an operating design gust wind speed $\widehat{U}_{op} = 30$ m/s at a 10 m height, whereas the maximum operating hinge moment with $\widehat{U}_{op} = 30$ m/s is 22% smaller than the stow hinge moment with $\widehat{U}_{st} = 40$ m/s in the suburban terrain. Lowering the operating design gust wind speed to 29 m/s in the desert terrain and increasing the operating design gust wind speed to 33 m/s in the suburban terrain ensures that the operating load is maximum while remaining below the stow load for all operating conditions of the heliostat. It is notable that the maximum operating loads at larger elevation angles, such as $\alpha \geq 45°$, are less than 60% and 70% of the stow load for the optimal operating design wind speeds of 29 m/s and 33 m/s in the desert and suburban terrains, respectively. This presents an opportunity to increase the design wind speed and thus the operating hours of those regions of the heliostat field with favourable configurations (e.g. $\alpha \geq 45°$) for reducing the maximum hinge moments without compromising the strength and mass of material in a heliostat design with drives that are able to resist the maximum loads in stow and operating positions.

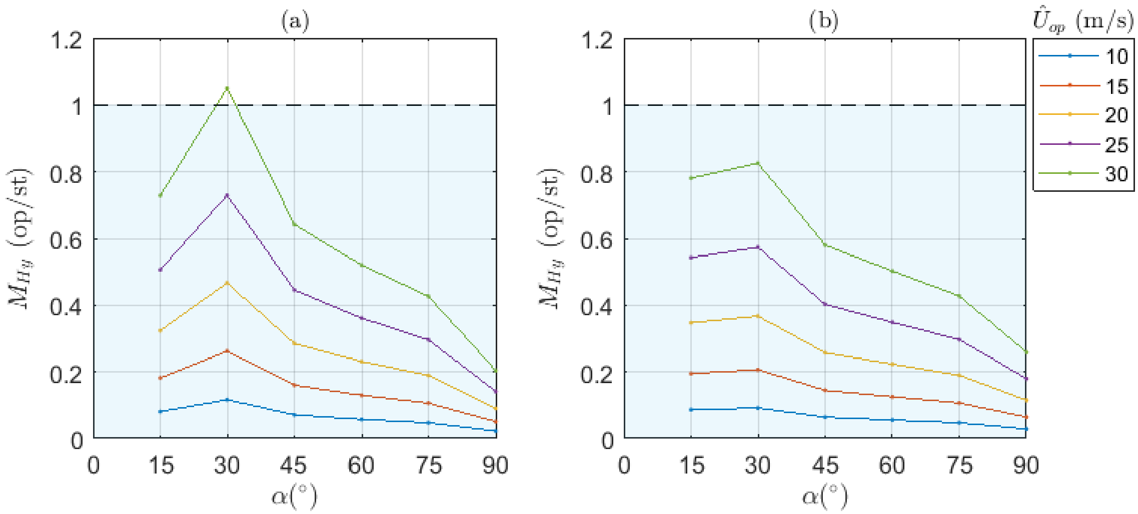

Figure 14. Ratios of the peak operating hinge moment to the stow ultimate design ($\widehat{U}_{st}$ = 40 m/s at z = 10 m) hinge moment M_{Hy} as a function of operating elevation angle α and maximum operational design wind speed ($\widehat{U}_{op}$ at z = 10 m) on a 6 m × 6 m heliostat with H/c = 0.5 positioned in: (a) flat desert with $\alpha_{\bar{U}}$ = 0.12, I_u = 13% and G_u = 1.44; (b) suburban terrain with $\alpha_{\bar{U}}$ = 0.2, I_u = 26% and G_u = 1.70.

Figure 15 presents the maximum operating overturning moments normalised with respect to the ultimate design stow overturning moments on a 6 m × 6 m heliostat with H/c = 0.5 as a function of elevation angle and operating design gust wind speed ($\widehat{U}_{op}$). It can be seen that the critical operating configuration of the heliostat is α = 90°, such that $\widehat{U}_{op}$ = 17 m/s in a flat desert (Figure 15a) and $\widehat{U}_{op}$ = 18 m/s in a suburban terrain (Figure 15b). It is relevant to consider that the heliostats are likely to only be operating at α close to 90° for small periods of the day near sunrise and sunset, which may lead to over-designed loads for the structural rigidity of the pedestal and the concrete depth of the foundation. For example, the operating design wind speed that allows the maximum operating load to remain below the stow load can be increased to 18 m/s in a flat desert and 21 m/s in a suburban terrain for the operating range of $\alpha \leq 45°$. As an example, the elevation angles of two heliostats positioned 100 m and 362 m to the north of a 100 m tower can differ by up to 15° when tracking throughout a day (Zeghoudi and Chermitti 2014). For a maximum gust wind speed of 20 m/s during a summer day (21 May to 22 July in northern hemisphere) from 8 am to 4 pm that would nominally stow the entire field in a suburban terrain (Figure 15b), the majority of in-field heliostats (100 m) close to the tower with α = 40-55° would need to be stowed. However, the heliostats in the outer region of the field (362 m) with α = 25-40° could continue to operate throughout this period. It should be noted that such a partial stowing strategy of the field can only be realised when the operating range of elevation angles is below the elevation angle corresponding to the maximum operating load ($\alpha = 90°$ for overturning moment). Despite the favourable working conditions for the overturning moment at smaller elevation angles, such a stowing strategy would need to be avoided for the operating hinge moment in Figure 14. This is because a transition to stow (of the order of minutes) in the event of increasing wind speed would expose the heliostat to the maximum operating hinge moment at $\alpha = 30°$ and potential structural failure. Characterisation of the dynamic effects, including torsional motions and displacements of the heliostat resulting from the critical wind load cases investigated in the current study, warrants further investigation to optimise the mass and cost of the heliostat support structure, pylon thickness and foundation depth.

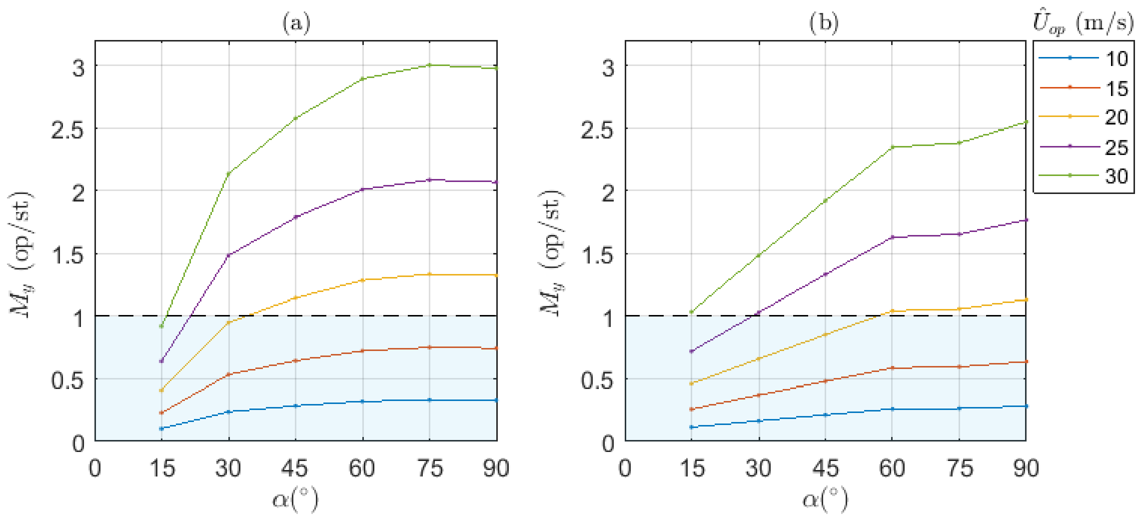

Figure 15. Ratios of the peak operating overturning moment M_y to the stow ultimate design ($\hat{U}_{st} = 40$ m/s at $z = 10$ m) overturning moment as a function of operating elevation angle α and maximum operational design wind speed ($\hat{U}_{op}$ at $z = 10$ m) on a 6 m × 6 m heliostat with $H/c = 0.5$ positioned in: (a) flat desert terrain with $\alpha_{\bar{U}} = 0.12$, $I_u = 13\%$ and $G_u = 1.44$; (b) suburban terrain with $\alpha_{\bar{U}} = 0.2$, $I_u = 26\%$ and $G_u = 1.70$.

4. Conclusions

The maximum loads caused by turbulent wind conditions during the operation of a heliostat field are an important design consideration to maximise the solar output of a power tower plant, while maintaining structural integrity and performance of the high-cost, wind-sensitive heliostat components, such as the drive units. The current study investigated the effect of the non-uniform pressure distribution at turbulence intensities and gust factors representing a flat desert and a suburban terrain according to the lowest 10 m of full-scale atmospheric boundary layer (ABL) data from the Engineering Sciences Data Unit (ESDU) 85020 model. It was found that the maximum hinge moment coefficient was strongly correlated to the position of the centre of pressure from the heliostat central elevation axis. The maximum lift coefficient was at $\alpha = 30°$ and $\beta = 0°$ in agreement with Peterka and Derickson (1992), whereas the maximum hinge moment coefficient was found at $\alpha = 15°$ and $\beta = 180°$ in a highly turbulent flow with 26% turbulence intensity due to a larger movement of the centre of pressure toward the leading edge with decreasing α. Furthermore, the movement of the centre of pressure on heliostats with $\alpha \leq 30°$ is larger at $\beta = 180°$ than at $\beta = 0°$. The increase in pressure on the lower surface of the heliostat is caused by the "ground effect" observed on wings and flat plates with $H/c \leq 0.5$ at small angles of attack. Hence, wind approaching the upward-facing ($\beta = 0°$) and downward-facing ($\beta = 180°$) surfaces of a heliostat in the operating range of $\alpha =$ 15-30° should be considered to determine the maximum hinge moment on the elevation drive of a conventional pedestal-mounted heliostat.

The maximum hinge and overturning moment coefficients on the heliostat in the current study were shown to follow a linear increase with the longitudinal turbulence of the approaching flow in the ABL. The peak hinge moment coefficient was highly correlated to the position of the centre of pressure and the elevation angle of the heliostat, whereas the overturning moment coefficient was largely dependent on the maximum drag force with the maximum frontal projected area of the heliostat surface to the wind. This is highlighted in the difference of the maximum movement of the centre of pressure increasing with decreasing elevation angle from approximately 5% of the heliostat chord length at $\alpha = 90°$ to more than 30% of the heliostat chord length in stow position ($\alpha = 0°$). With a doubling of turbulence intensity from 13% to 26%, the position of the centre of pressure due to the peak pressure distribution at $\alpha = 30°$ increases above the 10% threshold specified for square cross-section monoslope roofs with $\alpha = 30°$ in ASCE 7-02 (2002). The increased movement of the centre of pressure contributes to the maximum hinge moment coefficients of 0.65 at $\alpha = 30°$ and 0.76 at $\alpha = 15°$ for wind at $I_u = 26\%$ approaching the windward ($\beta = 0°$) and leeward ($\beta = 180°$) edges of the heliostat, respectively. The maximum hinge moments due to the centre of pressure movement investigated in the current study were based on a single heliostat size, however the effect of the turbulence length scales with respect to the heliostat dimensions warrants further investigation in future studies.

Application of the peak hinge moment coefficients on a 36 m^2 heliostat design, with drives that are able to resist the maximum loads in stow and operating positions, to full-scale ABL data showed that the maximum operational design wind speed can be increased to 29 m/s in a desert terrain and 33 m/s in a suburban terrain for an ultimate design stow wind speed of 40 m/s. However, the maximum operating loads at larger elevation angles $\alpha \geq 45°$ are less than 60% and 70% of the stow load for the same operating design wind speed specification in desert and suburban terrains, respectively. In contrast, the maximum operating design wind speed that allows the maximum operating overturning moment for $\alpha \leq 45°$ to remain below the stow load is 18 m/s in a flat desert and 21 m/s in a suburban terrain for the operating range of $\alpha \leq 45°$. This presents an opportunity to increase the operating hours of those regions of the heliostat field with favourable elevation-azimuth configurations that have smaller operating loads than the maximum stow loads and would not expose the heliostat to the maximum operating load during the transition to the stow position in the event of increasing wind speed. The methodology and results for deriving the hinge and overturning moments in the current study can form part of structural design considerations for determining the appropriate design wind speeds in different terrains and the critical heliostat configurations that lead to the maximum design wind loads on the elevation drive and foundation. The effects of turbulence intensity and the position of the centre of pressure on the design hinge and overturning moments are critical for the strength and stiffness of the elevation drive during operation and the structural rigidity of the pedestal and foundation in stow position.

Acknowledgements

The authors would like to acknowledge the financial support for the work within the Australian Solar Thermal Research Initiative (ASTRI) through funding provided by the Australian Renewable Energy Agency (ARENA).

References

AS/NZS 1170.2 (2011), “Structural Design Actions - Part 2: Wind actions”, Standards Australia and Standards New Zealand, Sydney.

ASCE 7-02 (2002), Minimum design wind loads for buildings and other structures, American Society of Civil Engineers, Reston, Virginia.

Durst, C.S. (1960), Wind speeds over short periods of time, Meteorological Magazine, 89(1960), 181-186.

Emes, M.J., Arjomandi, M., Ghanadi, F. and Kelso, R.M. (2017), Effect of turbulence characteristics in the atmospheric surface layer on the peak wind loads on heliostats in stow position, Solar Energy, 157, 284-297.

Emes, M.J., Arjomandi, M. and Nathan, G.J. (2015), Effect of heliostat design wind speed on the levelised cost of electricity from concentrating solar thermal power tower plants, Solar Energy, 115, 441-451.

Emes, M.J., Jafari, A., Ghanadi, F. and Arjomandi, M., 2019. A method for the calculation of the design wind loads on heliostats, in: SolarPACES, AIP Conference Proceedings, Casablanca, Morocco, pp. 030020.

EN 1991-1.4 (2010), Actions on structures, Part 1-4: General actions - Wind actions, Eurocode, Brussels.

ESDU 85020 (2001), Characteristics of atmospheric turbulence near the ground, Part II: single point data for strong winds (neutral atmosphere), Engineering Sciences Data Unit, London.

Ghanadi, F., Emes, M., Yu, J., Arjomandi, M. and Kelso, R., 2017. Investigation of the atmospheric boundary layer characteristics on gust factor for the calculation of wind load, in: SolarPACES 2016, AIP Conference Proceedings 1850, Abu Dhabi.

Gong, B., Wang, Z., Li, Z., Zang, C. and Wu, Z. (2013), Fluctuating wind pressure characteristics of heliostats, Renewable energy, 50, 307-316.

Holloran, M. and O'Meara, S. (1999), “Wing in ground effect craft review”, Defence Science and Technology Organisation, Canberra, Australia.

Holmes, J., Letchford, C. and Lin, N. (2006), Investigations of plate-type windborne debris—Part II: Computed trajectories, Journal of Wind Engineering and Industrial Aerodynamics, 94(1), 21-39.

Holmes, J.D. (2007), Wind loading of structures, Taylor & Francis, New York, USA.

IEA-ETSAP and IRENA (2013), Concentrating Solar Power Technology Brief.

Jafari, A., Ghanadi, F., Arjomandi, M., Emes, M.J. and Cazzolato, B.S. (2019a), Correlating turbulence intensity and length scale with the unsteady lift force on flat plates in an atmospheric boundary layer flow, Journal of Wind Engineering and Industrial Aerodynamics, 189, 218-230.

Jafari, A., Ghanadi, F., Emes, M.J., Arjomandi, M. and Cazzolato, B.S., 2018. Effect of Free-stream Turbulence on the Drag Force on a Flat Plate, in: AFMC, Adelaide, Australia.

Jafari, A., Ghanadi, F., Emes, M.J., Arjomandi, M. and Cazzolato, B.S. (2019b), Measurement of unsteady wind loads in a wind tunnel: scaling of turbulence spectra, Journal of Wind Engineering and Industrial Aerodynamics, 193, 103955.

Kolb, G.J., Ho, C.K., Mancini, T.R. and Gary, J.A. (2011), "Power tower technology roadmap and cost reduction plan", SAND2011-2419; Sandia National Laboratories, Albuquerque.

Kopp, G.A., Farquhar, S. and Morrison, M.J. (2012), Aerodynamic mechanisms for wind loads on tilted, roof-mounted, solar arrays, Journal of Wind Engineering and Industrial Aerodynamics, 111, 40-52.

Mendis, P., Ngo, T., Haritos, N., Hira, A., Samali, B. and Cheung, J. (2007), Wind loading on tall buildings, EJSE Special Issue: Loading on Structures, 3, 41-54.

Murphy, L.M. (1980), "Wind loading on tracking and field-mounted solar collectors", SERI-TP-632-958; Solar Energy Research Institute, Golden, USA.

Ortiz, X., Rival, D. and Wood, D. (2015), Forces and moments on flat plates of small aspect ratio with application to PV wind loads and small wind turbine blades, Energies, 8(4), 2438-2453.

Peterka, J.A. and Derickson, R.G. (1992), "Wind load design methods for ground-based heliostats and parabolic dish collectors", SAND92-7009; Sandia National Laboratories, Albuquerque, New Mexico.

Peterka, J.A., Tan, Z., Bienkiewicz, B. and Cermak, J. (1988), “Wind loads on heliostats and parabolic dish collectors: Final subcontractor report”, SERI/STR-253-3431; Solar Energy Research Institute, Golden, Colorado.

Peterka, J.A., Tan, Z., Cermak, J.E. and Bienkiewicz, B. (1989), Mean and peak wind loads on heliostats, Journal of Solar Energy Engineering, 111(2), 158-164.

Pfahl, A., Buselmeier, M. and Zaschke, M. (2011), Wind loads on heliostats and photovoltaic trackers of various aspect ratios, Solar Energy, 85, 2185-2201.

Pfahl, A., Coventry, J., Röger, M., Wolfertstetter, F., Vásquez-Arango, J.F., Gross, F., Arjomandi, M., Schwarzbözl, P., Geiger, M. and Liedke, P. (2017a), Progress in heliostat development, Solar Energy, 152, 3-37.

Pfahl, A., Gross, F., Liedke, P., Hertel, J., Rheinländer, J., Mehta, S., Vásquez-Arango, J.F., Giuliano, S. and Buck, R., 2017b. Reduced to Minimum Cost: Lay-Down Heliostat with Monolithic Mirror-Panel and Closed Loop Control, in: SolarPACES 2017, AIP Conference Proceedings 2033, Santiago.

Pfahl, A., Randt, M., Meier, F., Zaschke, M., Geurts, C. and Buselmeier, M. (2015), A holistic approach for low cost heliostat fields, Energy Procedia, 69, 178-187.

Simiu, E. and Scanlan, R.H. (1996), Wind Effects on Structures, John Wiley & Sons.

Téllez, F., Burisch, M., Villasente, Sánchez, M., Sansom, C., Kirby, P., Turner, P., Caliot, C., Ferriere, A., Bonanos, C.A., Papanicolas, C., Montenon, A., Monterreal, R. and Fernández, J. (2014), “State of the Art in Heliostats and Definition of Specifications”, 609837; STAGE-STE Project, Madrid.

Xu, Y.L. (2013), Wind Effects on Cable-Supported Bridges, John Wiley & Sons, Singapore.

Yu, J.S., Emes, M.J., Ghanadi, F., Arjomandi, M. and Kelso, R.M. (2019), Experimental investigation of peak wind loads on tandem operating heliostats within an atmospheric boundary layer, Solar Energy, 183, 248-259.

Zeghoudi, A. and Chermitti, A. (2014), Estimation of the Solar Power Tower Heliostat Position using Neural Network, International Journal of Computer Applications, 94(4), 41-46.